Crystal Structure and Atomic Vacancy Optimized Thermoelectric Properties in Gadolinium Selenides

Feiyu Qin,[1] Sergey Nikolaev,[2] Ady Suwardi,[3] Max Wood,[4] Yingcai Zhu,[4] Xianyi Tan,[3,5] Umut Aydemir,[6,7] Yang Ren,[8] Alex Yan Qingyu,[5] Lei Hu,[1,2,*] G. Jeffrey Snyder[4,*]

1. Institute of Innovative Research, Tokyo Institute of Technology, 4259 Nagatsuta, Midori-ku, Yokohama 226-8503, Japan
2. Laboratory for Materials and Structures, Tokyo Institute of Technology, 4259 Nagatsuta, Midori-ku, Yokohama 226-8503, Japan
3. Institute of Materials Research and Engineering, 2 Fusionopolis Way, Agency for Science, Technology and Research, Singapore 138634
4. Department of Materials Science and Engineering, Northwestern University, Evanston, IL 60208, United States
5. School of Materials Science and Engineering, Nanyang Technological University, Singapore 639798, Singapore
6. Department of Chemistry, Koc University, Sariyer, Istanbul, 34450, Turkey
7. Koc University Boron and Advanced Materials Application and Research Center, Sariyer, Istanbul-34450, Turkey
8. X-ray Science Division, Argonne National Laboratory, Argonne, Illinois 60439, United States

1. Abstract

Thermoelectric materials enable the mutual energy conversion of waste heat and electricity, critical to relieve global energy crisis. High-temperature thermoelectric materials are special species due to their high-temperature stability and noticeable energy conversion efficiency. Here, we report a systematic investigation on high-temperature thermoelectric gadolinium selenides, cubic $Gd_{3-x}Se_4$ (x = 0.16, 0.21 and 0.25) and orthorhombic Gd_2Se_{3-y} (y = 0.02, 0.06 and 0.08). High energy synchrotron x-ray diffraction and total scattering are used to investigate the crystallographic and local structures. The atomic-scale cluster of Gd vacancy in cubic $Gd_{2.84}Se_4$ is observed by employing the reverse Monte Carlo simulation. For cubic $Gd_{3-x}Se_4$, its carrier concentration is tuned and multiple conduction bands are incorporated by adjusting Gd vacancy. Experimentally, the gradual increase in effective masses is evidently observed in cubic $Gd_{3-x}Se_4$, which is consistent with the density functional theory (DFT) calculation. A reasonable peak zT value of 0.27 is achieved at 850 K for $Gd_{2.84}Se_4$. On the other hand, adjusting Se vacancy enables the optimization of electron concentration for orthorhombic Gd_2Se_{3-y} phase. Its low deformation potential (Ξ = 12eV) with single conduction band gives rise to enhanced electron mobility and higher peak zT value of 0.54 at 850 K for $Gd_2Se_{2.98}$. In addition, a higher zT of 1.2 at1200 K is reasonably predicted for $Gd_2Se_{2.98}$ by using

quality factor analysis. This work not just presents a systematic crystallographic investigation of gadolinium selenides, but also provides a deep insight into the charge transport and phonon scattering mechanisms. This study facilitates the exploration of more high-temperature thermoelectric materials.

2. Introduction

Thermoelectric materials are capable of harvesting the waste heat into electricity, which opens a new strategy to establish sustainable, renewable and clean energy sources and evolves into one of promising trends to resolve the urgent global energy crisis.[1,2] The energy transformation efficiency in thermoelectric semiconductors is determined by the dimensionless figure of merit, zT.[3] The zT is defined as $\frac{\alpha^2\sigma}{\kappa_e+\kappa_L}T$, where α is the Seebeck coefficient, σ is the electrical conductivity, T is the absolute temperature, κ_e and κ_L are electronic and lattice thermal conductivities, respectively.[4]

Since the Seebeck coefficient, electrical conductivity and electronic thermal conductivity are highly entwined by the charge carrier concentration (n),[5] physical strategies to enhance thermoelectric properties could be categorized into electronic band structure engineering, aiming at the promotion of power factor ($\alpha^2\sigma$), like band convergence in PbTe,[6,7] $CoSb_3$,[8] n-type Mg_3Sb_2,[9,10,11,12] and GeTe[13,14], resonant energy levels in PbTe:Tl,[15,16] band inversion in (Pb,Sn)(Te,Se),[17] and (Pb,Cr)Te[18], etc. In addition, another significant theme is to search for intrinsically low thermal conductivity, like SnSe[19,20,21] as well as superionic semiconductors Cu_2Se[22] and Ag_9GaSe_6[23], and to build up diverse phonon scattering centers extrinsically, such as introducing rattling phonon modes in open

frameworks in $Ba_8Ga_{16}Ge_{30}$ [24] and $AgBi_3S_5$, [25] and engineering hierarchical defect structures (atomic alloying, nanostructured inclusions and grain-boundary interfaces) to scatter phonons with full length scales.[26,27,28]

To promote energy conversion efficiency, a large temperature gradient is beneficial.[29] Hence, thermoelectric materials with higher operating temperatures are attractive, especially for radioisotope thermoelectric generators (RTGs) used in deep space missions. Until now, the high-temperature thermoelectric materials are scarce and limited in silicon germanium,[30] $Y_{14}MSb_{11}$ (M = Ca, Mn and Al),[31] half-heuslers,[32,33,34] and rare-earth metal chalcogenides, such as $R_{3-x}Te_4$ (R = La,[35,36] Pr[37] and Nd[38]). The rare-earth metal chalcogenides have been extensively investigated over the past decades.[39] Firstly, rare-earth (R) metal chalcogenides demonstrate complicated crystal structures with quite large number of atoms per unit cell, which means the large population of optical phonons and low phonon velocities. Secondly, cubic R_3X_4 (X = S, Se and Te) accommodates appreciable amount of cationic vacancy (up to 1/9), resulting in disordered structure and favorable for vacancy-phonon scattering. Thirdly, rare-earth metal chalcogenides are characteristic of high temperature melting point, such as 1992 K for $La_{3-x}Te_4$,**Error! Bookmark not defined.** and concomitantly large temperature gradient. The last but not the least, 4*f* electronic states of

rare earth element results in large density of states and thus enhanced Seebeck coefficient[37] (except for lanthanum chalcogenides with the f^0 in La^{3+}). Even though there are diverse rare earth metal chalcogenides reported. However, the accurate crystal structure, short-range local structure, charge transport and phonon scattering are still need to be investigated further.

Here we report high-temperature thermoelectric compounds cubic $Gd_{3-x}Se_4$ (x = 0.16, 0.21 and 0.25) and orthorhombic Gd_2Se_{3-y} (y = 0.02, 0.06 and 0.08). For cubic $Gd_{3-x}Se4$, the existence of atomic-scale cluster of Gd vacancy is observed experimentally by the reverse Monte Carlo simulation. By tuning the cationic vacancy in $Gd_{3-x}Se_4$, the effect of multiple conduction valleys is realized. Concomitantly, the effective masses also change from 0.9 m_e (m_e, free electron mass), to 1.1 m_e and finally to 1.4 m_e for $Gd_{3-x}Se_4$. The peak zT value is achieved to be 0.27 at 850 K for $Gd_{2.84}Se_4$. For orthorhombic Gd_2Se_{3-y}, the dominant single conduction band is consistent with the unchanged effective mass of 0.7 m_e. More significantly, lower deformation potential leads to higher mobility and thus the maximum zT value of 0.54 at 850 K for $Gd_2Se_{2.98}$. This work focuses on the accurate description of crystal structure, localized disorder, charge transport and phonon scattering in gadolinium selenides, which provides a good reference for understanding high-temperature thermoelectric materials.

3. Crystal structures

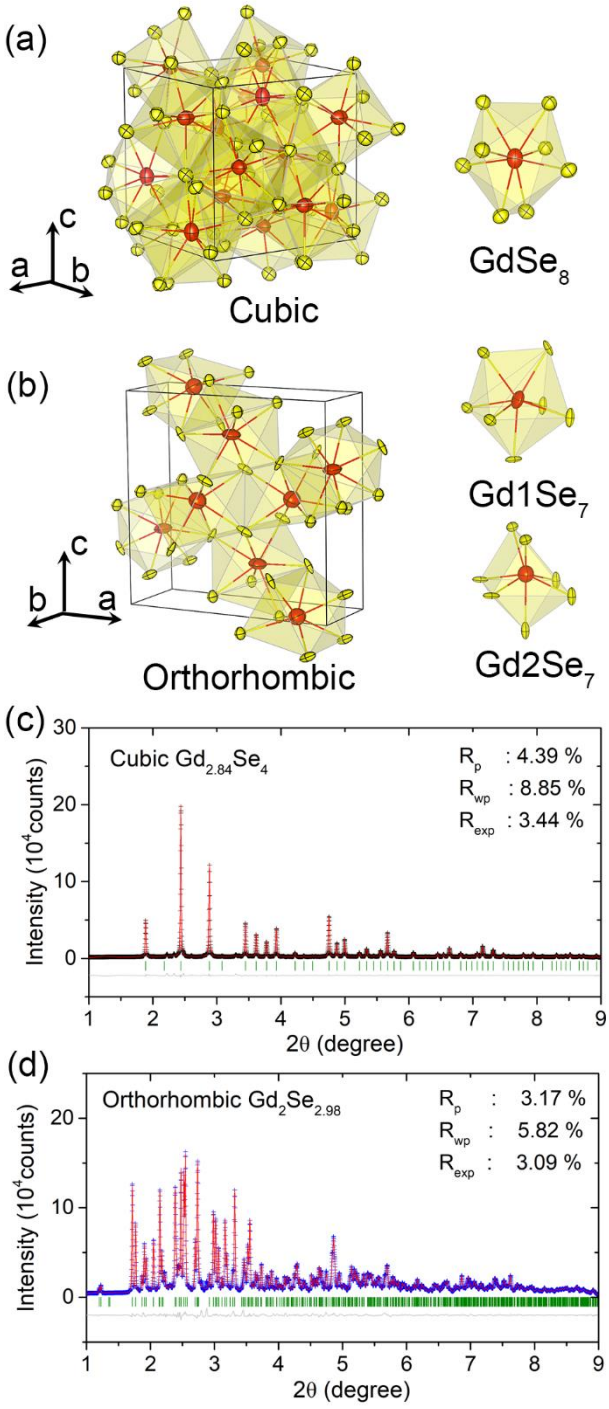

Figure1. (a) Crystal structure of cubic Gd_3Se_4, which consists of $GdSe_8$ polyhedron depicted in the right panel. (b) Crystal structure of orthorhombic Gd_2Se_3, composed of two different $GdSe_7$ polyhedral units (right panel). The Gd and Se are shown by the thermal ellipsoids, which is extracted from structure refinement. Rietveld structure refinement of synchrotron x-ray diffraction patterns of (a) cubic $Gd_{2.84}Se_4$, and (b) orthorhombic $Gd_2Se_{2.98}$. The insets demonstrate corresponding goodness of fit, R_p, R_{wp} and R_{exp}.

By tuning the stoichiometry of Gd and Se, we prepared a series of gadolinium selenides, cubic $Gd_{3-x}Se_4$ (x = 0.16, 0.21 and 0.25) and orthorhombic Gd_2Se_{3-y} (y = 0.02, 0.06 and 0.08). The chemical compositions were investigated by energy dispersive X-ray spectroscopy (EDS), as shown in Table S1. The cubic $Gd_{3-x}Se_4$ crystallizes in the Th_3P_4-type structure. Gd is eightfold coordinated with Se, forming trigonal dodecahedra (Figure 1a). In Figure 1a, the Gd (red) and Se (yellow) are shown by the thermal ellipsoids, quantitatively based on the atomic displacement parameters (ADPs) from Rietveld structure refinement of synchrotron x-ray diffraction data (SXRD). And its orthorhombic counterparts, Gd_2Se_{3-y} is isostructural with Sb_2S_3 (Stibnite), with 2 different Gd and 3 distinct Se crystallographic sites. These Gd atom is coordinated with seven Se anions, forming edge-sharing decahedra (Figure 1b). To obtain the precise crystallographic structure information, Rietveld structure refinements of SXRD patterns of $Gd_{3-x}Se_4$ and Gd_2Se_{3-y} were performed according to the cubic ($I\bar{4}3d$) and orthorhombic (*Pnma*) symmetries. The short wavelength of 0.11730 Å of synchrotron x-ray guarantees high resolution of diffraction patterns and high precision of refined structure parameters. It is clearly seen that the calculated diffraction profile (red lines in Figure 1c and 1d) of $Gd_{2.84}Se_4$ and $Gd_2Se_{2.98}$ agree well with the experimental diffraction patterns (black and blue crosses). This consistency is also confirmed by the reasonable values of goodness of fit (R_p, R_{wp} and

R_{exp}), shown in the inset of Figure 1c and 1d. The Rietveld structure refinements of SXRD of other compositions are presented in Figure S2. And the structure parameters, including the lattice constant, coordination fraction and atomic displacement parameters, etc. are tabulated in Table S2 and S3.

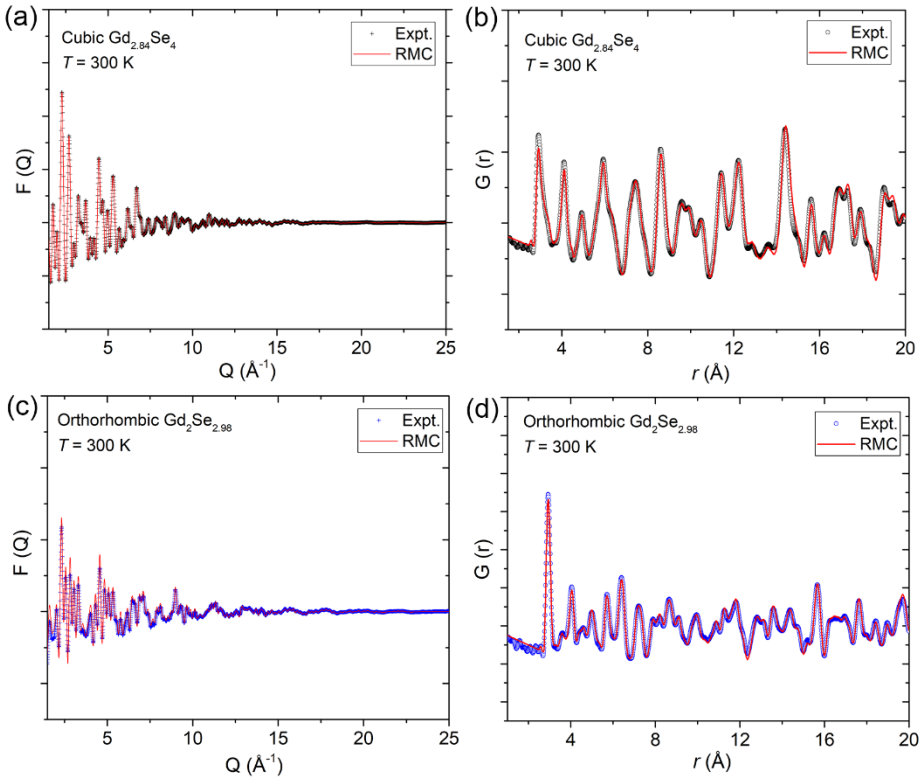

Figure2. Reverse Monte Carlo (RMC) fit to (a) F(Q) and (b) G(r) functions for cubic $Gd_{2.84}Se_4$. RMC fit to (c) F(Q) and (d) G(r) functions for orthorhombic $Gd_2Se_{2.98}$. The cross and circle demonstrate experimental data and the solid lines are RMC simulation.

To investigate the local disorder of cubic $Gd_{3-x}Se_4$ and orthorhombic Gd_2Se_{3-y}, reverse Monte Carlo (RMC) fits were performed on RMCprofile[40] using the initial atomic configurations of 6×6×6 supercell of cubic model and 6×15×6 supercell of orthorhombic model. The fits are constrained by simulating the experimental reciprocal and real space data, structure factor F(Q) and pair distribution function G(r). As shown in

Figure 2a, the RMC fits to cubic $Gd_{2.84}Se_4$ and orthorhombic $Gd_2Se_{2.98}$ provide satisfactory simulation to the F(Q) and G(r) functions. The G(r) functions of other compositions, PDFgui[41] fit and partial G(r) functions of atomic-pairs, like Gd-Gd, Gd-Se and Se-Se, are presented in Figure S3. The initial atomic configuration for RMC fit comes from the PDFgui fit, shown in FigureS3b and S3e.

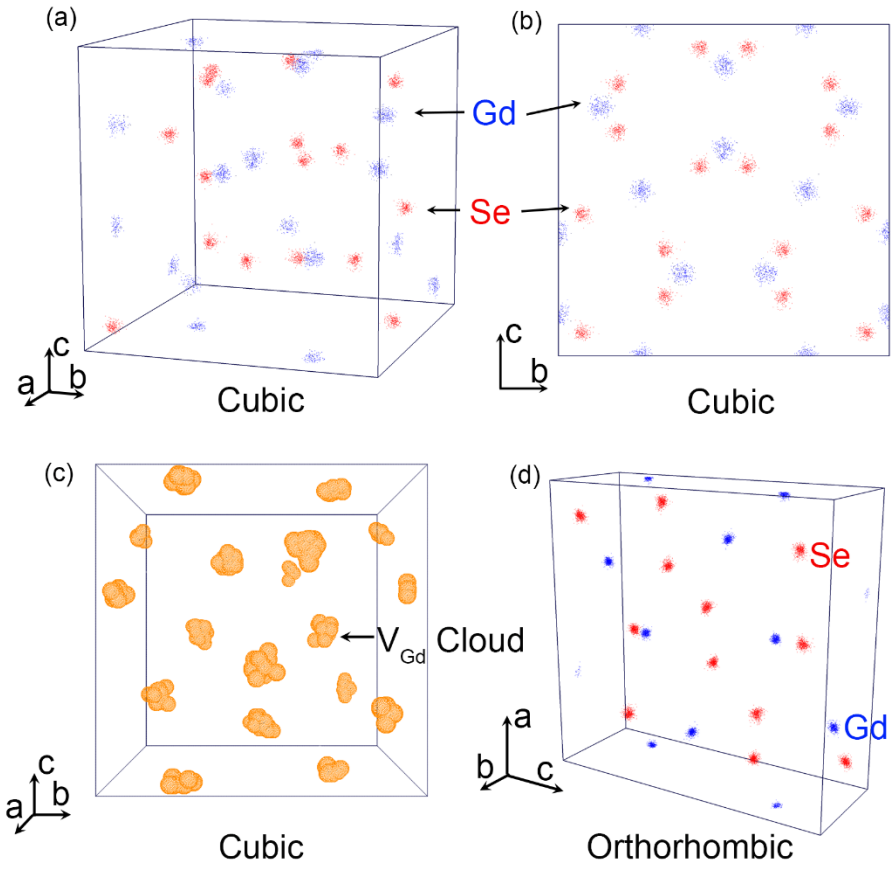

Figure3. (a) and (b) Atomic arrangements of cubic $Gd_{2.84}Se_4$, (c) Gd vacancy distribution shown by the orange clusters, and (d) atomic arrangement of orthorhombic $Gd_2Se_{2.98}$. Gd and Se atoms are shown in blue and red colors. RMC fits of a 6×6×6 supercell of cubic model (6048 atoms) and a 6×15×6 supercell of orthorhombic model (10 800 atoms). The cubic model is constructed with a certain proportion of Gd vacancy (5 mol%), which is confirmed by the pair distribution function refinement.

The RMC atomic arrangements of cubic $Gd_{2.84}Se_4$ were constructed based on the $I\bar{4}3d$ symmetry with an approximate 5 mol% Gd vacancy.

This initial configuration is confirmed by the small-box refinement on G(r) function by using PDFgui. Close inspection reveals that Gd and Se atoms scatter away from their equilibrium positions to form anisotropic distributions. Especially, the atomic cloud of Gd (blue) is apparently larger than that of Se atomic cloud (red) as shown in Figure 3a and 3b, confirming the significant local disorder of heavier Gd atoms. This larger local disorder found in Gd atoms than that of Se atoms is also consistent with the large ADP for Gd atoms (0.015 $Å^2$), in contrast to ADP of Se atoms (0.012 $Å^2$). Furthermore, the distribution of Gd vacancy is highlighted by the irregular aggregates in orange color as shown in Figure 3c. It is apparent that the Gd vacancy clusters are separated from each other with the distance of several angstroms in the unit cell. This atomic-scale cluster of Gd vacancy seems to play significant roles in scattering carrier and phonon transport. On the other hand, for the orthorhombic $Gd_2Se_{2.98}$, the Gd and Se atoms form compact and isotropic-like atomic cloud as presented in Figure 3d.

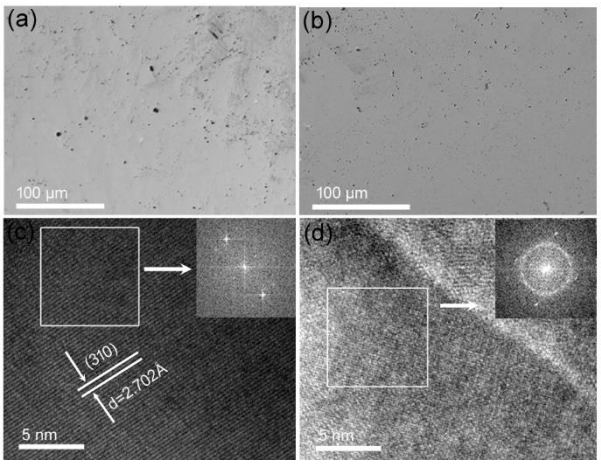

Figure4. SEM images of (a) cubic $Ga_{2.84}Se_4$ and (b) orthorhombic $Gd_2Se_{2.98}$, HRTEM images of (c) $Gd_{2.84}Se_4$ and (d) $Gd_2Se_{2.98}$. The fast fourier transformation (FFT) patterns in the top-right corners of (c) and (d) correspond to areas marked by white square.

To investigate the microstructural features of cubic $Gd_{2.84}Se_4$ and orthorhombic $Gd_2Se_{2.98}$, scanning electron microscopy (SEM) and high-resolution transmission electron microscopy (HRTEM) were performed. As shown in Figure 4a and 4b, cubic $Gd_{2.84}Se_4$ and orthorhombic $Gd_2Se_{2.98}$ demonstrate a high degree of homogeneous compositions, confirmed by the indiscernible contrast. The dark spots in Figure 4a and 4b are attributed to the porosity formed in the long-term hot-pressing process. Figure 4c shows the clear lattice fringe with the distance of 2.702 Å, which corresponds to the (310) crystal plane of cubic $Gd_{2.84}Se_4$. And the sharp diffraction pattern in the inset demonstrates its high crystallinity. In Figure 4d, the grain boundary is clearly observed, while no nanoscale crystal imperfections, like nanoscale dislocations and precipitates, is detected.

4. Electronic band structures

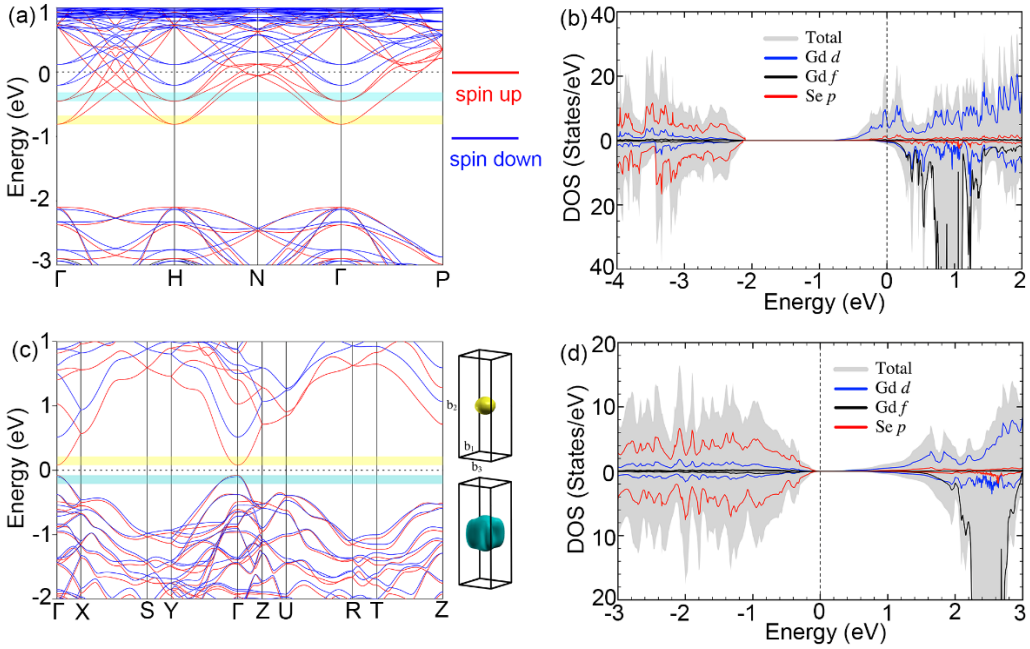

Figure5. (a) DFT-calculated electronic band structure (red: spin up; blue: spin down), and (b) atomic orbital projected density of states (DOS) of cubic Gd_3Se_4 with spin polarization. (c) Band structure (left panel), and Fermi surfaces of conduction band (the upper of right panel) and valence band (the bottom of right panel) of orthorhombic Gd_2Se_3. (d) The DOS of orthorhombic Gd_2Se_3. The Fermi level, (E_f) is set to zero energy (dotted line). In (b) and (d), the total and atomic orbital projected DOS are shown by the gray shadow and lines in different colors. The Fermi surfaces in yellow and green colors, correspond to the E_f away from the band edges with 0.1 eV, as demonstrated by the yellow and blue bars in (c). The b1, b2 and b3 in (c) are the reciprocal cell vectors.

To provide a deeper insight into the electronic charge transport in the following section, the density functional theoretical calculations were performed with considering spin polarization, due to the magnetic order of cubic R_3Se_4 (rare earth) and orthorhombic Gd_2Se_3.[42,43] The calculation details are presented in the supporting information. Electronic band structure of cubic Gd_3Se_4 is shown in Figure 5a. It is apparent that the Fermi level (dot line) cuts deeply into the conduction band, in accordance with the electronic band structures reported in R_3Te_4 (R = La, Pr and

Nd).[35,37,38] Since the Gd^{3+} donates 3 electrons and the Se^{2-} only accepts 2 electrons to form Gd-Se chemical bonds, this leads to one free electron per unit formula and accounts for its intrinsically metallic characteristic. Besides, multiple conduction bands are observed separately situating at the Γ point of Brillouin zone with different band offsets. For cubic Gd_3Se_4, the total density of states (DOS, gray shadow) around the conduction band bottom, is primarily composed of Gd *d*-states (blue line), hybridized with Se *p*-states as presented in Figure 5b. And the Gd *f*-states (black line) dominate the DOS above E_f (dotted line). The DOS of valence band mainly originates from Se *p*-states (red line), hybridized with Gd *d*-states and a small proportion of Gd *f*-states.

In Figure 5 c for orthorhombic Gd_2Se_3, the conduction band minimum (CBM) is located at Γ point. And the secondary conduction band along Γ-Z-U line stays away from the primary band at Γ point with approximate 0.6 eV of band offset. The Fermi surface corresponding to the CBM demonstrates an ellipsoid shape, showing anisotropic electron transport feature. In contrast, the valence band maximum (VBM) at Γ point reveals slightly flattened feature, implying a larger effective mass than that of the CBM. And the $E \sim k$ dispersions along Γ-Z and Γ-Y are highly asymmetric, consistent with the distorted Fermi surface, as shown in the bottom of right panel of Figure 5c. Analogous to the case of Gd_3Se_4, the Gd *d*-states in orthorhombic Gd_2Se_3 is dominant in the CBM, while the Gd *f*-states locate

around higher energy region. The effect of electronic correlations in the Gd *f* shell was considered by using the rotationally invariant generalized gradient approximation, GGA+*U* scheme[44] with $U = 4$ eV. Electronic band structure and DOS calculated without on-site U are also presented in Figure S4 and S5.

5. Thermoelectric transport properties

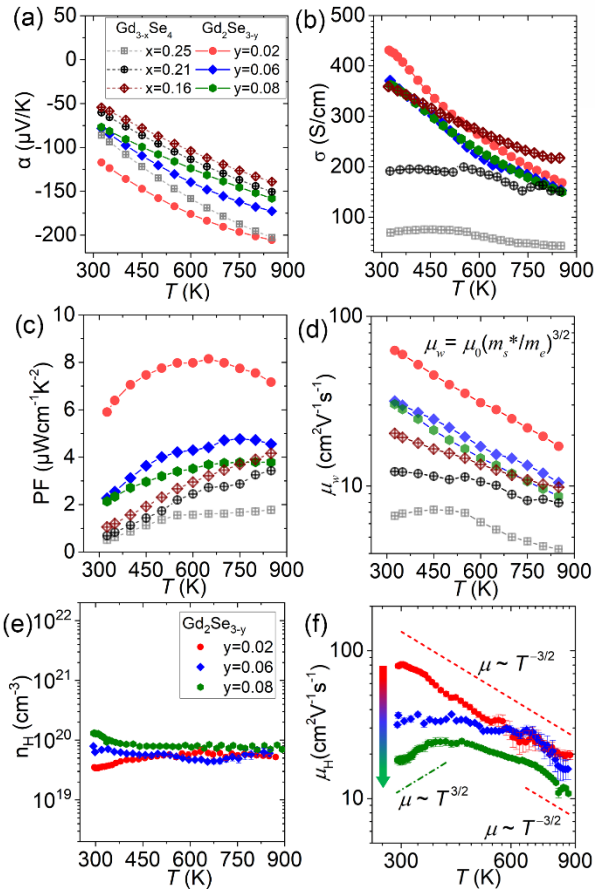

Figure6. Temperature dependence of (a) Seebeck coefficient, (b) electrical conductivity, (c) power factor, (d) weighted mobility, μ_w, (e) Hall carrier concentration n_H, and (f) Hall mobility, μ_H. In (d) and (e), only n_H and μ_H of Gd_2Se_{3-y} are presented.

The temperature dependence of Seebeck coefficient (α) and electrical conductivity (σ) for the cubic $Gd_{3-x}Se_4$ (x = 0.16, 0.21 and 0.25) and orthorhombic Gd_2Se_{3-y} (y = 0.02, 0.06 and 0.08) are presented in Figure 6a and 6b. All compositions are *n*-type semiconductors, as suggested by the negative α values. With the temperature rising, the magnitude of Seebeck coefficient, |α| shows a monotonous increase trend while σ declines for all samples, demonstrating the characteristic of degenerate semiconductors. With increasing the content of Gd vacancy, x from 0.16 to 0.25 for $Gd_{3-x}Se_4$, |α| increases from 54 μV/K to 86 μV/K at room temperature (RT)

while the σ values decreases from 359.1 S/cm to 69.5 S/cm, mainly due to the drops in electron concentration (Figure S6a). By contrast, with increasing Se vacancy, y in Gd_2Se_{3-y}, |α| is suppressed from 117 μV/K to 77 μV/K for y = 0.02 and 0.08 at room temperature (RT). Simultaneously, the σ values change from 431.9 S/cm to 362.4 S/cm. In cubic $Gd_{3-x}Se_4$, power factor (PF) increases with raising temperature and reaches a peak value of 4.2 $\mu Wcm^{-1}K^{-2}$ at 850 K for x = 0.16 (Figure 6c). For orthorhombic $Gd_2Se_{2.98y}$, PF firstly increases and then form a maximum value of 8.1 $\mu Wcm^{-1}K^{-2}$ around 650 K, followed by a continuous decline. The weighted mobility, $\mu_w = \mu_0(m_s^*/m_e)^{3/2}$, is independent of carrier concentration and closely correlated with the electrical performance of thermoelectric materials. In Figure 6d, the orthorhombic Gd_2Se_{3-y} shows higher μ_w, compared to the cubic counterparts. And for the $Gd_2Se_{2.98}$, its μ_w (red dots) changes from 62.9 cm^2/Vs at RT down to 17.2 cm^2/Vs at 850 K.

The large fluctuations of n_H and μ_H in cubic $Gd_{3-x}Se_4$ brings challenges to analyze the transport behavior (Figure S6), so we here just focus on orthorhombic Gd_2Se_{3-y}. In orthorhombic Gd_2Se_{3-y}, n_H demonstrates a subtle variation with increasing temperature (Figure 6e). For y = 0.02, μ_H declines with increasing temperature in a $T^{-3/2}$ tendency, exhibiting a dominant acoustic phonon (APS) scattering throughout the entire temperature range (Figure 6f). And for y = 0.06, μ_H remains almost constant below 425 K. Distinctly, for y = 0.08, μ_H gradually increases in $T^{3/2}$ way below 425 K,

and reduces in $T^{-3/2}$ trend at high temperatures. Below 425 K, this obvious change in temperature exponent of μ_H implies an evolution from APS to a mixed scattering and ultimately to ionized impurity scattering (IIS). This variation of carrier scattering mechanisms has a close relationship with the progressive increase of Se vacancy in Gd_2Se_{3-y} compounds.

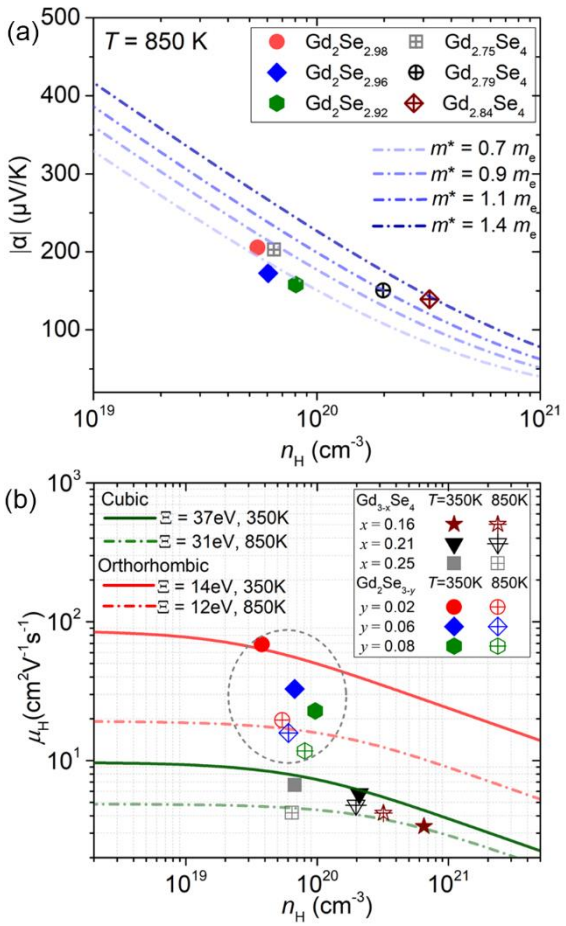

Figure7. (a) Seebeck coefficient and (b) Hall mobility as a function of Hall carrier concentration in cubic $Gd_{3-x}Se_4$ and orthorhombic Gd_2Se_{3-y}. In (a), the different effective masses are shown in gradually varied colors, indicated by the color bar. In (b), the lines indicate the mobility calculated based on the single parabolic band (SPB) model with assuming the dominating acoustic phonon scattering. For clarity, the deformation potential, Ξ of two-end temperatures, 350 and 850 K, is presented in the top-left corner. The red ellipsoid marks the mobilities of orthorhombic compositions.

To further understand the charge transport, effective mass analysis and Hall mobility investigation were performed. The Seebeck coefficient (|α|) and mobility (μ_H) as a function of Hall carrier concentration (n_H) of cubic $Gd_{3-x}Se_4$ and orthorhombic Gd_2Se_{3-y} were investigated. At high temperatures, the APS dominates at all compositions, already confirmed by the temperature dependence of Hall mobility in Figure 6f. The Pisarenko lines (|α| *vs* n_H) based on the single parabolic band (SPB) model

with different DOS effective masses, m_s* are presented in Figure 7a. It is clearly seen that the reduction of Seebeck coefficient |α| from low to high n_H in orthorhombic Gd_2Se_{3-y} (solid symbols) is consistent with the single band model with $m_s^* = 0.7\ m_e$ (m_e, free electron mass). However, Seebeck coefficient in $Gd_{3-x}Se_4$ compounds move to higher m_s^* from 0.9 m_e for x = 0.25, to 1.1 m_e for x = 0.21 and finally to 1.4 m_e for x = 0.16, with gradually increasing n_H (empty symbols). The evident increase in m_s^* demonstrates multiple conduction valleys involved, when the Fermi level is pushed up into conduction bands by changing Gd vacancy. The change of m_s^* with cationic vacancy is also observed in $La_{3-x}Te_4$.[35,36]

Here we assume that the APS dominates electron transport in the SPB model. Within the approximation, the Hall mobility μ_H and n_H are listed by equation (1) and (2).

$$\mu_H = \frac{e}{\sqrt{2}m_I^*}\frac{\pi\hbar^4 v_l^2 d}{\Xi^2 (m_b^* k_B T)^{3/2}}\frac{(1/2+2\lambda)F_{2\lambda-1/2}}{(1+\lambda)F_\lambda} \quad (1)$$

$$n_H = \frac{8\pi}{3}\left(\frac{2m_s^* k_B T}{h^2}\right)^{3/2}\frac{(1+\lambda)^2 F_\lambda^{\,2}}{(1/2+2\lambda)F_{2\lambda-1/2}} \quad (2)$$

Here $\hbar$ is the reduced Planck constant, k_B is Boltzmann constant, v_l is longitudinal speed of sound, d is sample density, F_j is Fermi integral, m_I^* is inertial mass, m_b^* is single-band effective mass, m_s^* is DOS effective mass ($m_s^*=N_v^{2/3}m_b^*$, N_v band degeneracy), Ξ is deformation potential and λ is scattering parameter (for APS, λ=0).

Hall mobility, μ_H as a function of electron concentration n_H of $Gd_{3-x}Se_4$ and Gd_2Se_{3-y} at 350 K (solid line) and 850 K (dot line) are depicted in Figure 7b. Here the lines are calculated by equations (1) and (2) based on the hypothetical isotropic conduction band. It is evident that the orthorhombic compounds, encircled by a gray ellipsoid, demonstrate higher μ_H (red lines in Figure 7b) than these of cubic counterparts (olive lines) throughout the whole carrier concentration range. For instance, the μ_H of 68.9 $cm^2V^{-1}s^{-1}$ for $Gd_2Se_{2.98}$ at 350 K, is one order higher than that of $Gd_{2.84}Se_4$ with μ_H = 6.7 $cm^2V^{-1}s^{-1}$. With increasing temperature to 850 K, the APS dominates and the μ_H in $Gd_2Se_{2.98}$ decreases to 19.6 $cm^2V^{-1}s^{-1}$, still higher than that of $Gd_{2.84}Se_4$ (4.2 $cm^2V^{-1}s^{-1}$). The higher mobility in orthorhombic phases originate from the low Ξ, such as Ξ = 12 eV compared to Ξ = 31 eV for the cubic counterpart at 850 K, as shown in the inset of Figure 6b. This deformation potential characterizes the degree of carrier scattered by lattice thermal vibration (phonon). [45] The smaller deformational potential demonstrates weak perturbation on carrier mobility and are favorable for thermoelectric performances. The mobilities observed at 350 K of Gd_2Se_{3-y} (y = 0.06 and 0.08) deviate away from the calculated lines. This discrepancy is presumably due to the ionized impurity scattering (λ = 2), which has been observed in Figure 6f.

6. Thermal conductivity and phonon scattering

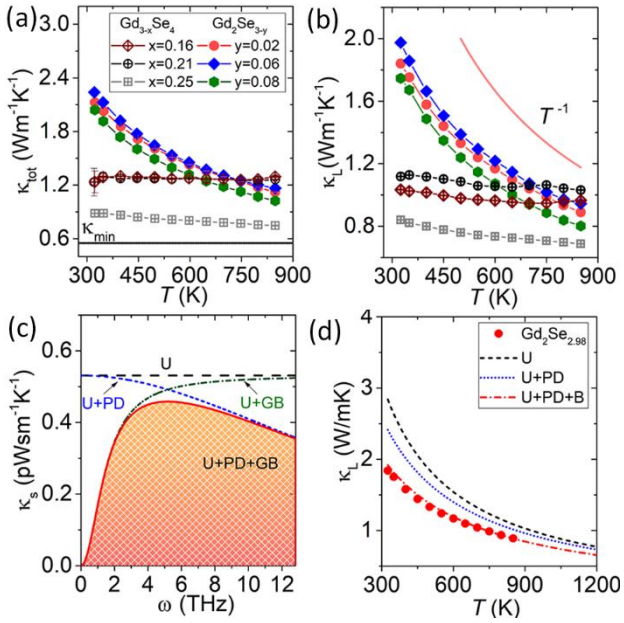

Figure8. (a) Total thermal conductivity, κ_{tot}, (b) lattice thermal conductivity, κ_L of cubic $Gd_{3-x}Se_4$ and orthorhombic Gd_2Se_{3-y} compounds, (c) phonon frequency (ω) dependence of spectral thermal conductivity, κ_s based on different phonon scattering mechanisms. U, PD, GB denote phonon-phonon Umklapp process, point defect scattering and grain boundary scattering for $Gd_2Se_{2.98}$ at 850 K. (d) Temperature-dependent observed (red symbol) and calculated (lines) κ_L for $Gd_2Se_{2.98}$.

Temperature dependence of total thermal conductivity, κ_{tot} and lattice thermal conductivity, κ_L for cubic $Gd_{3-x}Se_4$ and orthorhombic Gd_2Se_{3-y} are presented in Figure 8a and 8b. The κ_L was calculated by subtracting the electronic contribution, κ_e from total thermal conductivity. The κ_e is calculated by using the Wiedemann-Franz law, $\kappa_e = L\sigma T$, in which σ is the electrical conductivity and L is the Lorenz number depicted in FigureS7. The κ_{tot} and κ_L of cubic $Gd_{3-x}Se_4$ show slight decrease tendency, strongly departing from the acoustic phonon dominated T^{-1} relationship. For instance, the κ_L of $Gd_{2.84}Se_4$ decreases from 1.03 W/mK at RT to 0.97 W/mK at 850 K with only 6 % reduction. Given that the absence of

nanoscale imperfections confirmed by microstructural investigation in Figure4, the peculiar temperature dependent κ_L should strongly correlate with the Gd vacancy. This cationic vacancy forms the atomic-scale cluster, confirmed by the RMC investigation in Figure 3c, presumably plays a significant role in suppressing phonon transport. This strong cationic vacancy phonon scattering has also been discussed in SnTe-$AgSbTe_2$ solid solution.[46]

In contrast, κ_L in orthorhombic Gd_2Se_{3-y} diminishes substantially with increasing temperature. For instance, κ_L in $Gd_2Se_{2.98}$ decreases from 1.84 W/mK (325K) to 0.89 W/mK (850K) with a fall of ~52 percentage. It is worth noting that this κ_L reduction is close to the T^{-1} tendency depicted by the red line in Figure 8b, demonstrating a predominant Umklapp scattering of acoustic phonons.

To elucidate the origin of the reduced κ_L in $Gd_{3-x}Se_4$ and Gd_2Se_{3-y}, a series of physical parameters were collected and calculated, tabulated in TableS4. Generally, the larger Grüneisen parameter, γ implies stronger lattice anharmonicity and lower intrinsic lattice thermal conductivity. The γ values of cubic $Gd_{2.84}Se_4$ and orthorhombic $Gd_2Se_{2.98}$ are 1.69 and 1.63 respectively, comparable to elaborately designed $La_{3-x}Te_4$ ($\gamma = 1.72$)[35,36] and $Pr_{3-x}Te_4$ ($\gamma = 1.62$),[37] listed in Table S4. The Debye temperature, θ_D of $Gd_{2.84}Se_4$ and $Gd_2Se_{2.98}$ are 251 K and 265 K, higher than these of rare earth metal tellurides (θ_D = 208 K). It is reasonable that smaller atomic mass of

selenium produces larger acoustic phonon cut-off frequency and thus higher average sound velocities. And their κ_{min} are 0.58 W/mK for $Gd_{2.84}Se_4$ and 0.56 W/mK for $Gd_2Se_{2.98}$, which is comparable to that of $La_{3-x}Te_4$ (κ_{min} = 0.50 W/mK)[35] and $Pr_{3-x}Te_4$ (κ_{min} = 0.51 W/mK).[37]

According to the Debye-Callaway model, we could investigate different phonon scattering mechanisms in Gd_2Se_{3-y} samples.

$$\kappa_L = \frac{k_B}{2\pi^2 v_m}\left(\frac{k_B T}{\hbar}\right)^3 \int_0^{\theta_a/T} \frac{\tau_{total}(x)x^4 e^x}{(e^x-1)^2}dx \quad (3)$$

Where θ_a is the modified Debye temperature considering structural complexity ($\theta_a = \theta_D/N^{1/3}$), and x is $\hbar\omega/k_BT$. τ_{total} is the total relaxation time, which is the reciprocal sum of relaxation time of distinct phonon scattering mechanisms, for instance τ_U (Umklapp phonon-phonon scattering, U), τ_{PD} (point defect scattering, PD), and τ_{GB} (grain boundary scattering, GB), etc. The spectral thermal conductivity, κ_s is provided in Figure 8c. The area under the curve of k_s as a function of ω is positively proportional to κ_L. It is evident that the Umklapp process scatters all-wavelength acoustic phonons. Point defects play a significant role in suppressing phonon transport in high frequency region. And grain boundary cuts low-frequency phonons. The modeled κ_L of orthorhombic $Gd_2Se_{2.98}$ is presented in Figure 8d by taking account of Umklapp phonon-phonon, point defect and grain boundary scattering. With progressively introducing phonon scattering mechanisms, the modeled κ_L with U, PD and GB shown by the red line has a good agreement with the experimental κ_L (red points). Here we only

provide the thermoelectric measurement up to 850 K, due to the limit of measurement devices. However, the gadolinium selenides are densified by hot pressing at 1200 K during 2 hours, which enables their high temperature stability, such as $La_{3-x}Te_4$ suitable for 1200 K and $Pr_{3-x}Te_4$ working at 1273 K.[35,37] Consequently, we extend this κ_L simulation up to 1200 K and obtain a reasonably predicted κ_L of 0.66 W/mK for $Gd_2Se_{2.98}$. The parameters used for this modeling is presented in the phonon scattering section in the supporting information.

7. Figure of merit, *zT* and quality factor, *B*

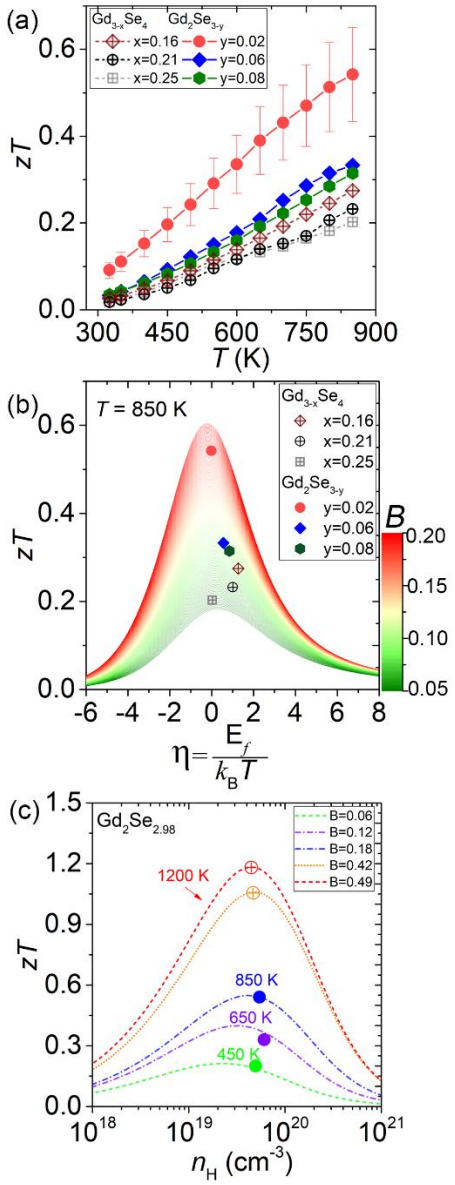

Figure9. Figure of merit, *zT* as a function of (a) temperature for cubic $Gd_{3-x}Se_4$ and orthorhombic Gd_2Se_{3-y}, (b) *zT* (*T* = 850 K) versus reduced chemical potential, η. The quality factors, the *B* values from 0.05 to 0.20 stack in continuously varied colors. (c) Hall carrier concentration, n_H, dependence of *zT* for orthorhombic $Gd_2Se_{2.98}$ at different temperatures. The error bar of *zT* for $Gd_2Se_{2.98}$ is estimated to be 20 %. The filled circles are experimental data and the cross circles are predicted values at 1200 K. The simulated lines correspond to distinct *B* values listed in the top-right concern of Figure 9c.

As shown in Figure 9a, *zT* of both cubic $Gd_{3-x}Se_4$ and orthorhombic Gd_2Se_{3-y} increases gradually with raising temperature. A maximum *zT* of 0.27 at 850 K is achieved for cubic $Gd_{2.84}Se_4$. Orthorhombic phases

demonstrate higher zT values and the peak zT of 0.54 emerges for $Gd_2Se_{2.98}$ at 850 K, comparable to these representative high-temperature thermoelectric materials, like $La_{3-x}Te_4$ (zT ~ 0.45 at 850K),[35] $Ca_{0.97}Na_{0.03}AlSb_3$ (zT ~ 0.48 at 850K)[47] and SiGe (zT ~ 0.63 at 850K).[36] This detailed zT comparison is presented in Figure S8.

In order to understand the origin in zT optimization, zT *versus* η (reduced chemical potential) is presented in Figure 9b with a series of quality factor, B from 0.05 to 0.20. At the optimized η, usually locating at band edge, zT monotonously enhances with promoting B. The quality factor is favorable for analyzing and predicting thermoelectric performance, since it decouples the tunable carrier concentration and intrinsic physical parameters, as shown by the following equations.[5]

$$zT = \frac{\alpha^2(\eta)}{\frac{(k_B/e)^2}{B \cdot F_0(\eta)} + L(\eta)} \quad (4)$$

$$B = \frac{2\hbar k_B^2}{3\pi} \cdot \frac{v_l^2 dN_V T}{m_I^* \Xi^2 \kappa_L} \quad (5)$$

As shown in Figure 9b, the enhancement of zT in cubic $Gd_{3-x}Se_4$ and orthorhombic Gd_2Se_{3-y} is predominantly attributed to the improvement of B values, which boosts from B = 0.06 to 0.09 for x = 0.25 to x = 0.16 in the cubic $Gd_{3-x}Se_4$. And it rises from B = 0.10 to 0.18 for the orthorhombic Gd_2Se_{3-x} (y = 0.08 and 0.02, respectively) at 850 K. The improvement of quality factors for cubic $Gd_{3-x}Se_4$ is mainly due to multiple conduction valleys, confirmed by the gradual increases in m_s^* from 0.9 m_e to 1.4 m_e. For the orthorhombic Gd_2Se_{3-y}, the zT promotion is primarily attributed to

the optimized mobilities, given that only single conduction band dominates. Essentially, this enhanced mobility originates from the lower deformation potential, like 12 eV for $Gd_2Se_{2.98}$.

The Hall carrier concentration, n_H dependence of zT for orthorhombic $Gd_2Se_{2.98}$ is also depicted in Figure 9c. the zT values at elevated temperatures, are calculated based on SPB model, which is highly in accordance with the experimental data (circles in Figure 9c). The optimal carrier concentration is nearly achieved in the composition of $Gd_2Se_{2.98}$ at 850 K by tuning Se deficiency. Here, we employ the quality factors of B = 0.42 and 0.49 to reasonably predict the zT values at 1200 K. As shown in Figure 9c, the highest zT could be achieved to 1.1 and 1.2 at 1200 K. This B values are calculated based on the intrinsic physical parameters, including v_L, N_v, m_s^*, Ξ and κ_L, by using the equation (5). For the B of 0.42, we use the κ_L of 0.66 W/mK at 1200 K, which is obtained from the Debye-Callaway modeling to the experimental parameters as shown in Figure 8d. And for B = 0.49, we use the minimum κ_L of 0.56 W/mK in $Gd_2Se_{2.98}$ calculated by the Cahill estimation.[48]

8. Conclusion

In summary, a systematic study on crystal structure and thermoelectric properties of cubic $Gd_{3-x}Se_4$ (x = 0.16, 0.21 and 0.25) and orthorhombic Gd_2Se_{3-y} (y = 0.02, 0.06 and 0.08) are reported here. Their complicated crystal structures are investigated by the Rietveld structure refinement of synchrotron x-ray diffraction patterns. For the cubic phase, by tuning Gd vacancy, electron concentration is optimized and multiple conduction bands are involved, accompanying with the gradual improvement of effective masses, m_s^* from 0.9 m_e to 1.4 m_e. These multiple valleys give rise to a reasonable zT value of 0.27 at 850 K for cubic $Gd_{2.84}Se_4$. The Gd vacancy in $Gd_{3-x}Se_4$ forms the atomic-scale cluster, confirmed by the RMC simulation. For the orthorhombic Gd_2Se_{3-y}, the increase in Se vacancy introduces more electrons while its effective mass keeps unchanged to be 0.7 m_e, showing only single conduction band behind. Intriguingly, it demonstrates the deformation potential Ξ, as low as 12 eV. This low Ξ guarantees higher carrier mobility and thus a promising zT value of 0.54 at 850 K for $Gd_2Se_{2.98}$. By using the quality factor analysis, the maximum zT of $Gd_2Se_{2.98}$ could be achieved up to 1.2 at 1200 K. This work presents a deep understanding on the crystal structure, short-range local structure, charge transport and phonon scattering mechanisms of gadolinium selenides, which facilitate the exploration of promising high-temperature thermoelectric materials.

9. Supporting information

The detailed experimental procedures, like ball milling, hot pressing, the measurement of thermoelectric properties (Seebeck coefficient, electrical conductivity, Hall coefficient, and speed of sound, etc), as well as the physical models of charge transport and phonon scattering, are presented in the supporting information.

10. Acknowledgements

The authors would like to acknowledge EFRC Solid-State-Thermal Energy Conversion Center (S3TEC), Grant DE-SC000XXXX. This work is also supported by Japan Society for the Promotion of Science (JSPS) KAKENHI, Grant JP 19F19057. L. H. acknowledge the International Research Fellow of JSPS. Q. F. Y. acknowledge the Chinese Scholarship Council (CSC) for the scholarship in Tokyo Institute of Technology. A. Q. Yan acknowledges Singapore MOE Tier 2 under Grant MOE2018-T2-1-010. Use of the Advanced Photon Source was supported by the U.S. Department of Energy, Office of Science, Office of Basic Energy Science, under Contract No. DE-AC02-06CH11357.

11.Conflicts of Interest

The authors declare no confict of interest.

12.References

1 Snyder G. J., Toberer E. S. Complex thermoelectric materials. *Nature*

Materials. **2008**, 7, 105–114.

2 Tan G., Zhao L. D., Kanatzidis M. G. Rationally designing high performance bulk thermoelectric materials. *Chemical Review.* **2016**, 116, 12123-12149

3 Pei Y., Wang H., Snyder G. J. Band engineering of thermoelectric materials. *Advanced Materials*. **2012**, 24(46):6125-35.

4 Pei Y., LaLonde A. D., Wang H., Snyder G. J. Low effective mass leading to high thermoelectric performance. *Energy & Environmental Science.* **2012**, 5(7), 7963-9.

5 Kang S. D., Snyder G. J. Transport property analysis method for thermoelectric materials: material quality factor and the effective mass model. *arXiv preprint arXiv:1710.06896*. **2017**, 18.

6 Pei Y., Shi X., LaLonde A., Wang H., Chen L., Snyder G. J. Convergence of electronic bands for high performance bulk thermoelectrics. *Nature*. **2011**, 473(7345):66.

7 Pei Y., LaLonde A., Iwanaga S., Snyder G. J. High thermoelectric figure of merit in heavy hole dominated PbTe. *Energy & Environmental Science*. **2011**, 4(6):2085-9.

8 Tang Y., Gibbs Z. M., Agapito L. A., Li G., Kim H. S., Nardelli M. B., Curtarolo S., Snyder G. J. Convergence of multi-valley bands as the electronic origin of high thermoelectric performance in $CoSb_3$ skutterudites. *Nature Materials*. **2015**, 14(12):1223.

9 Tamaki H., Sato H. K., Kanno T. Isotropic Conduction Network and Defect Chemistry in $Mg_{3+\delta}Sb_2$-Based Layered Zintl Compounds with High Thermoelectric Performance. *Advanced Materials*. **2016**, 28, 10182–10187

10 Zhang J., Song L., Pedersen S. H., Yin H. L., Hung T., Iversen B. B.

Discovery of high-performance low-cost n-type Mg_3Sb_2-based thermoelectric materials with multi-valley conduction bands. *Nature Communications*. **2017**, 8, 13901.

11 Ohno S., Imasato K., Anand S., Tamaki H., Kang S. D., Gorai P., Sato H. K., Toberer E. S., Kanno T., Snyder G. J. Phase boundary mapping to obtain n-type Mg_3Sb_2-based thermoelectrics. *Joule*. **2018**, 2(1):141-54.

12 Imasato K., Kang S. D., Ohno S., Snyder G. J. Band engineering in Mg_3Sb_2 by alloying with Mg_3Bi_2 for enhanced thermoelectric performance. *Materials Horizons*. **2018**, 5(1), 59-64.

13 Zhang, X., Bu, Z., Lin, S., Chen, Z., Li, W., Pei, Y. GeTe Thermoelectrics. *Joule*. **2020**, 4., 1-18.

14 Hong, M., Zou, J., Chen, Z. G. Thermoelectric GeTe with diverse degrees of freedom having secured superhigh performance. *Advanced Materials*, **2019**, *31*(14), 1807071.

15 Heremans J. P., Jovovic V., Toberer E. S., Saramat A., Kurosaki K., Charoenphakdee A., Yamanaka S., Snyder G. J. Enhancement of thermoelectric efficiency in PbTe by distortion of the electronic density of states. *Science*. **2008**, 25, 321(5888):554-7.

16 Wiendlocha B. Thermopower of thermoelectric materials with resonant levels: PbTe:Tl versus PbTe:Na and $Cu_{1-x}Ni_x$. *Physical Review B*. **2018**, 9, 97(20):205203.

17 Xiao Y., Wang D., Qin B., Wang J., Wang G., Zhao L. D. Approaching topological insulating states leads to high thermoelectric performance in n-type PbTe. *Journal of the American Chemical Society*. **2018**, 140(40):13097-102.

18 Chen L. C., Chen P. Q., Li W. J., Zhang Q., Struzhkin V. V., Goncharov A. F., Ren Z. F., Chen X. J. Enhancement of thermoelectric

performance across the topological phase transition in dense lead selenide. *Nature Materials*, **2019**, *18*(12), 1321-1326.

19 Zhao L. D., Lo H. S., Zhang Y., Sun H., Tan G., Uher C., Wolverton, C., Dravid V. P., Kanatzidis M. G. Ultralow thermal conductivity and high thermoelectric figure of merit in SnSe crystals. *Nature*, **2014**, *508*(7496), 373.

20 Li C. W., Hong J., May A. F., Bansal D., Chi S., Hong T., Ehlers G., and Delaire O. Orbitally driven giant phonon anharmonicity in SnSe. *Nature. Physics*, **2015**, *11*(12), 1063.

21 Chang, C., Wu, M., He, D., Pei, Y., Wu, C. F., Wu, X., Yu, H., Zhu, F., Wang, K., Chen, Y., Huang, L. Li, J., He, J., Zhao, L. D. 3D charge and 2D phonon transports leading to high out-of-plane ZT in n-type SnSe crystals. *Science*, **2018**, *360*(6390), 778-783.

22 Liu H., Shi X., Xu F., Zhang L., Zhang W., Chen L., Li Q., Uher C., Day T., Snyder G. J. Copper ion liquid-like thermoelectrics. *Nature Materials.* **2012**, 11(5):422.

23 Lin S., Li W., Li S., Zhang X., Chen Z., Xu Y., Chen Y., Pei Y. High thermoelectric performance of Ag_9GaSe_6 enabled by low cutoff frequency of acoustic phonons. *Joule.* **2017**, 1(4):816-30.

24 Christensen M., Abrahamsen A. B., Christensen N. B., Juranyi F., Andersen N. H., Lefmann K., Andreasson J., Bahl C. R., Iversen B. B. Avoided crossing of rattler modes in thermoelectric materials. *Nature Materials.* **2008**, 7(10):811.

25 Tan G., Hao S., Zhao J., Wolverton C., Kanatzidis M. G. High thermoelectric performance in electron-doped $AgBi_3S_5$ with ultralow thermal conductivity. *Journal of the American Chemical Society.* **2017**, 139(18):6467-73.

26 Zhao L. D., Hao. S, Lo. SH, Wu C., Zhou X., Lee Y., Li H., Biswas K., Hogan T. P., Uher C., Wolverton C., Dravid, V.P., Kanatzidis, M. G. High thermoelectric performance via hierarchical compositionally alloyed nanostructures. *Journal of the American Chemical Society.* **2013**, 135(19):7364-70.

27 Wu Y., Chen Z., Nan P., Xiong F., Lin S., Zhang X., Chen Y., Chen L. D., Ge, B. H., Pei, Y. Lattice strain advances thermoelectrics. *Joule*, **2019**, *3*(5), 1276-1288.

28 Luo Y., Cai S., Hao S., Pielnhofer F., Hadar I., Luo Z. Z., Xu J.W., Wolverton C., Dravid P. V., Pfitzner A., Yan Q. Y., Kanatzidis M. G. High-performance thermoelectrics from cellular nanostructured $Sb_2Si_2Te_6$. *Joule*, **2020**, *4*(1), 159-175.

29 Zhu T, Liu Y, Fu C, Heremans J. P., Snyder J. G, Zhao X. Compromise and synergy in high-efficiency thermoelectric materials. *Advanced Materials.* **2017**, 29(14):1605884.

30 Joshi G., Lee H., Lan Y., Wang X., Zhu G., Wang D., Gould R. W., Cuff D. C., Tang M. Y., Dresselhaus M. S., Chen G. Enhanced thermoelectric figure-of-merit in nanostructured p-type silicon germanium bulk alloys. *Nano Letters.* **2008**, 8(12):4670-4.

31 Toberer E. S., Cox C.A., Brown S. R., Ikeda T., May A. F., Kauzlarich S. M., Snyder G. J. Traversing the metal-insulator transition in a Zintl phase: rational enhancement of thermoelectric efficiency in $Yb_{14}Mn_{1-x}Al_xSb_{11}$. *Advanced Functional Materials.* **2008**, 18(18):2795-800.

32 Liu Y., Fu C., Xia K., Yu J., Zhao X., Pan H., Felser C., Zhu T. Lanthanide Contraction as a Design Factor for High-Performance Half-Heusler Thermoelectric Materials. *Advanced Materials*. **2018**, 30

(32):1800881.

33 Zhu H., He R., Mao J., Zhu Q., Li C., Sun J., Ren W., Wang Y., Liu Z., Tang Z., Sotnikov A. Discovery of ZrCoBi based half Heuslers with high thermoelectric conversion efficiency. *Nature Communications*. **2018**, 9(1):2497.

34 Zhu, H., Mao J., Li Y., Sun J., Wang Y., Zhu Q., Li G., Son Q., Zhou J., Fu Y., He R., Tong T., Liu Z., Ren W., Li Y., Wang Z., Luo J., Sotnikov A., Bao J., Nielsch K., Chen G., Singh D., Ren Z.F. Discovery of TaFeSb-based half-Heuslers with high thermoelectric performance. *Nature Communications*, **2019**, *10*(1), 1-8.

35 May A. F., Fleurial J. P., Snyder G. J. Thermoelectric performance of lanthanum telluride produced via mechanical alloying. *Physical Review B*, **2008**, *78*(12), 125205.

36 May A. F., Fleurial J. P., Snyder G. J. Optimizing thermoelectric efficiency in $La_{3-x}Te4$ via Yb substitution. *Chemistry of Materials*, **2010**, *22*(9), 2995-2999.

37 Cheikh D., Hogan B. E., Vo T., Von Allmen P., Lee K., Smiadak D.M., Zevalkink A., Dunn B. S., Fleurial J. P., Bux S. K. Praseodymium Telluride: A High-Temperature, High-ZT Thermoelectric Material. *Joule*. **2018**, 2(4):698-709.

38 Gomez S. J., Cheikh D., Vo T., Von Allmen P., Lee K., Wood M., Snyder G.J., Dunn B. S., Fleurial J. P., Bux S. K. Synthesis and Characterization of Vacancy-Doped Neodymium Telluride for Thermoelectric Applications. *Chemistry of Materials*. **2019**, 31:4460-8.

39 Wood C. High-temperature thermoelectric energy conversion-II. Materials survey. Energy conversion and management. 1984, 24(4):331-43.

40 Tucker M. G., Keen D. A., Dove M. T., Goodwin A. L., Hui Q. RMCProfile: reverse Monte Carlo for polycrystalline materials. *Journal of Physics: Condensed Matter*, **2007**, *19*(33), 335218.

41 Farrow C., Juhas P., Liu J.; Bryndin D., Božin E., Bloch J., Proffen T., Billinge, S. PDFfit2 and PDFgui: computer programs for studying nanostructure in crystals. *Journal of Physics: Condensed Matter*. **2007**, *19*, 335219.

42 Holtzberg F., McGuire T. R., Methfessel S., Suits J. C. Ferromagnetism in Rare-Earth Group VA and VIA Compounds with Th_3P_4 Structure. *Journal of Applied Physics*. **1964**, 35, 1033-8.

43 Guertin R. P, Foner S., Cooper B. R., Siemann R. Magnetic properties of an induced ferromagnet, Pr_3Se_4, under hydrostatic pressure. *Journal of Magnetism and Magnetic Materials*. **1980**,15:11-2.

44 Dudarev S. L., Botton G. A., Savrasov S. Y., Humphreys C. J., Sutton, A. P. Electron-energy-loss spectra and the structural stability of nickel oxide: An LSDA+U study. *Phys. Rev. B.* **1998**, **57**, 1505.

45 Herring, C., Vogt, E. Transport and deformation-potential theory for many-valley semiconductors with anisotropic scattering. *Physical Review*, **1956**, *101*(3), 944.

46 Tan G., Hao S., Hanus R. C., Zhang X., Anand S., Bailey T. P., Rettie A. J., Su X., Uher C., Dravid V. P., Snyder G. J. High Thermoelectric Performance in SnTe–$AgSbTe_2$ Alloys from Lattice Softening, Giant Phonon–Vacancy Scattering, and Valence Band Convergence. *ACS Energy Letters.* **2018**, 3(3):705.

47 Zevalkink A., Toberer E. S., Zeier W. G., Flage-Larsen E., Snyder G. J. Ca_3AlSb_3: an inexpensive, non-toxic thermoelectric material for waste heat

recovery. *Energy & Environmental Science*, **2011**, *4*(2), 510-518.

48 Cahill, D. G., Watson, S. K., Pohl, R. O. Lower limit to the thermal conductivity of disordered crystals. *Physical Review B*, **1992**, *46*(10), 6131.